



## Article (refereed) – Published version

---

Hughes, Chris W.; Elipot, Shane; Morales Maqueda, Miguel Angel; Loder, John W.. 2013 Test of a method for monitoring the geostrophic meridional overturning circulation using only boundary measurements. *Journal of Atmospheric and Oceanic Technology*, 30. 789-809. [10.1175/JTECH-D-12-00149.1](https://doi.org/10.1175/JTECH-D-12-00149.1)

This version available at <http://nora.nerc.ac.uk/500462/>

NERC has developed NORA to enable users to access research outputs wholly or partially funded by NERC. Copyright and other rights for material on this site are retained by the rights owners. Users should read the terms and conditions of use of this material at

<http://nora.nerc.ac.uk/policies.html#access>

© Copyright 2013 American Meteorological Society (AMS).

Permission to use figures, tables, and brief excerpts from this work in scientific and educational works is hereby granted provided that the source is acknowledged. Any use of material in this work that is determined to be “fair use” under Section 107 of the U.S. Copyright Act September 2010 Page 2 or that satisfies the conditions specified in Section 108 of the U.S. Copyright Act (17 USC §108, as revised by P.L. 94-553) does not require the AMS’s permission.

Republication, systematic reproduction, posting in electronic form, such as on a web site or in a searchable database, or other uses of this material, except as exempted by the above statement, requires written permission or a license from the AMS. Additional details are provided in the AMS Copyright Policy, available on the AMS Web site located at (<http://www.ametsoc.org/>) or from the AMS at 617-227-2425 or [copyrights@ametsoc.org](mailto:copyrights@ametsoc.org).

Contact NOC NORA team at  
[publications@noc.soton.ac.uk](mailto:publications@noc.soton.ac.uk)

## Test of a Method for Monitoring the Geostrophic Meridional Overturning Circulation Using Only Boundary Measurements

CHRIS W. HUGHES, SHANE ELIPOT, AND MIGUEL ÁNGEL MORALES MAQUEDA

*National Oceanography Centre, Liverpool, United Kingdom*

JOHN W. LODER

*Fisheries and Oceans Canada, Bedford Institute of Oceanography, Dartmouth, Nova Scotia, Canada*

(Manuscript received 23 July 2012, in final form 3 December 2012)

### ABSTRACT

Measurements of ocean bottom pressure, particularly on the continental slope, make an efficient means of monitoring large-scale integrals of the ocean circulation. However, direct pressure measurements are limited to monitoring relatively short time scales (compared to the deployment period) because of problems with sensor drift. Measurements are used from the northwest Atlantic continental slope, as part of the Rapid Climate Change (RAPID)–West Atlantic Variability Experiment, to demonstrate that the drift problem can be overcome by using near-boundary measurements of density and velocity to reconstruct bottom pressure differences with accuracy better than 1 cm of water (100 Pa). This accuracy permits the measurement of changes in the zonally integrated flow, below and relative to 1100 m, to an accuracy of 1 Sv ( $1 \text{ Sv} \equiv 10^6 \text{ m}^3 \text{ s}^{-1}$ ) or better. The technique employs the “stepping method,” a generalization of hydrostatic balance for sloping paths that uses geostrophic current measurements to reconstruct the horizontal component of the pressure gradient.

### 1. Introduction

Of the many parameters that can be measured to monitor the ocean circulation, ocean bottom pressure (OBP) is one that has a number of advantages, and one great disadvantage. The most obvious advantage is the fact that it is directly related to the dominant part of the flow (outside boundary layers): the geostrophic flow. Two OBP measurements at the same depth and latitude on the continental slope, but on opposite sides of an ocean basin, will measure the zonally integrated northward mass transport per unit depth. The integral is across the entire ocean basin at that depth. In an idealized, flat-bottomed ocean, such measurements would be thought of as sidewall pressure rather than bottom pressure. In the real ocean with sloping sidewalls, the sides are also the bottom; it is simply a matter of interpretation.

A second advantage is that of integrating right to the boundary. As a result, there is no difficulty associated

with recirculations. An integral of the mass transport from the boundary to a given point in the interior may produce a highly time-dependent result simply because the interior point is at different times on either one side or another of a meandering current, or inside/outside an eddy or other local recirculation. This has the potential to result in very large, stochastic variability of little relevance to the large scale (Wunsch 2008). For example, the western boundary arrays described by Toole et al. (2011) and Schott et al. (2006), while perfectly fine on their own terms as a system for monitoring the variability within the western boundary region itself, cannot be interpreted as being representative of the zonally integrated flow. When integrating from boundary to boundary, there is no possibility of aliasing recirculations that straddle the edge of the region, meaning that the stochastic variability tends to be reduced.

A third advantage of OBP relates to the part it plays in the depth-integrated vorticity balance, in which it appears in the form of the bottom pressure torque. This is associated with the gradient of pressure along a depth contour on sloping topography, and hence with vertical velocities (e.g., Hughes and de Cuevas 2001). The associated dynamical control on OBP gradients means that

---

*Corresponding author address:* Chris W. Hughes, National Oceanography Centre, Joseph Proudman Building, 6 Brownlow St., Liverpool L3 5DA, United Kingdom.  
E-mail: cwh@noc.ac.uk

gradients of OBP over a sloping boundary tend to be significantly smaller than pressure gradients in nearby interior eddies. This point will be discussed in more detail in a paper to follow (C. W. Hughes et al. 2013, unpublished manuscript), but it can be thought of as a generalization of the similar boundary suppression of eddy variability discussed by Kanzow et al. (2009) for the case of an ocean with vertical sidewalls.

These points would make OBP an ideal parameter to monitor in order to measure the meridional overturning circulation (MOC) were it not for one important problem: the pressure signals of interest are of order 1 cm of water equivalent, but even the best instruments are prone to drifts of order several centimeters per year or larger (Watts and Kontoyiannis 1990). However, given that we are considering an overturning circulation that, by its very nature, has a zonal integral that varies with depth, we can make progress by focusing on how the boundary pressure changes as a function of depth. In the case of a vertical sidewall, that would be particularly simple: hydrostatic balance allows us to calculate the change with depth simply from a measurement of density at the boundary, and this is the strategy used at other latitudes to measure the “interior” ocean transport between points just offshore of the continental slope (Send et al. 2011; Johns et al. 2008). On a sloping boundary, extra information is required. On such a boundary, at constant latitude  $y$ , OBP can be thought of as a function of the horizontal zonal coordinate  $x$ , with the vertical coordinate  $z = -H(x)$  being a function of  $x$ . This is the usual “looking down” viewpoint for which the seafloor is mapped onto a horizontal surface. Alternatively, we can think of OBP as a function of  $z$ , with  $x = X(z)$  on that surface, taking a viewpoint in which we are effectively looking to the west at the ocean’s western sidewall from a point within the ocean. Here, we map OBP onto the  $(y, z)$  plane instead of the  $(x, y)$  plane. From this point of view, we can think of how OBP varies as a function of  $z$ , but we must bear in mind that as  $z$  changes, we are actually following the sloping seafloor, and so there will be an associated change in  $x$ , which will be small for steep slopes but large for gentle slopes.

This means that the vertical gradient of OBP is not only given by the density but also involves the horizontal pressure gradient. For a geostrophic flow, that horizontal pressure gradient can be determined from a local current measurement. With these two measurements, density and current, it is then possible to determine how OBP changes with depth on a section across the continental slope. We have an analog of the hydrostatic balance, but along a sloping rather than vertical boundary.

The West Atlantic Variability Experiment (WAVE) was set up as part of the Rapid Climate Change (RAPID) experiment to demonstrate these concepts in the context

of monitoring the North Atlantic MOC. In particular, an array of bottom pressure recorders, current meters, and conductivity–temperature–depth (CTD) instruments were deployed in 2008 on the Canadian Atlantic continental slope at about  $42^{\circ}$ – $43^{\circ}$ N, on an extension of the Halifax section (Loder et al. 2003), referred to as the RAPID-Scotian (RS) Line. In this paper, we explain the theory in more detail, present measurements from the first year of deployment, and demonstrate that variations in pressure differences over a depth range of over 2750 m can be reconstructed using density and current measurements to within 1 hPa (1 hPa = 100 Pa = 1 mbar and is approximately equivalent to 1 cm of water). Elsewhere (Elipot et al. 2013), we apply the method detailed here to investigate the coherence between signals measured at and near the RS Line, and MOC-related measurements at other latitudes. A future paper will compare observations with ocean model predictions, focusing on the suppression of eddy variability on the continental slope, and the vertical structures of observed and modeled variability (C. W. Hughes et al. 2013, unpublished manuscript).

It is worth mentioning at this point that we are focusing purely on the Eulerian MOC, by which we mean the MOC as determined by zonally integrated transports at constant depth. To determine buoyancy or heat fluxes, one would be interested in the MOC calculated in density or temperature coordinates. At lower latitudes, where density and temperature contours are closer to horizontal, these are tightly related to the Eulerian MOC, but at the latitude we are considering, there is a significant decoupling. For example, the heat flux due to the horizontal “gyre” circulation can be as important as that associated with the Eulerian MOC (Marsh et al. 2009). On the other hand, the concept of “the” MOC as a large-scale, long-period mode of circulation in the Atlantic associated with deep-water formation in the north, is one that is typically associated with an Eulerian overturning streamfunction that spans the ocean from its southern limit to northern subpolar regions, and is associated with a heat transport that varies more strongly with latitude than does the flow itself, as illustrated, for example, in Figs. 1 and 3 of Marsh et al. (2009). The version of the MOC that is of interest depends on the question being asked.

## 2. Theoretical development

The integral quantity we are interested in is the zonally integrated northward mass transport per unit depth:

$$T(y, z) = \int_W^E \rho v dx, \quad (1)$$

where  $W(y, z)$  is the  $x$  coordinate of the western boundary of the ocean at depth  $z$  and meridional coordinate value

$y$ , and  $E(y, z)$  is the corresponding  $x$  coordinate of the eastern boundary. The coordinates  $(x, y, z)$  are in the directions (east, north, up), respectively. We will consider this integral in the light of the geostrophic relationship

$$\rho f \mathbf{k} \times \mathbf{u}_g = \rho f (-\mathbf{i}v_g + \mathbf{j}u_g) = -\nabla_h p, \quad (2)$$

where  $\mathbf{u}_g$  is the geostrophic horizontal velocity;  $f$  is the Coriolis parameter;  $(\mathbf{i}, \mathbf{j}, \mathbf{k})$  are unit vectors in the  $(x, y, z)$  directions, respectively;  $p$  is pressure; and  $\nabla_h$  represents the horizontal gradient operator. A zonal integral of the zonal component of (2) then leads to

$$T_g(y, z) = \int_W^E \rho v_g dx = \frac{p_E(y, z) - p_W(y, z)}{f}, \quad (3)$$

where  $T_g$  is the geostrophic component of  $T$ , and  $p_E$  and  $p_W$  are OBP at the eastern and western boundaries, respectively. Thus, as long as the geostrophic transport dominates, the net northward transport at each depth is determined simply by the difference between the eastern and western boundary pressures at a given depth and latitude. As shown in an ocean model context by Bingham and Hughes (2008), this does indeed appear to be the case over most of the ocean depth, with the near-surface Ekman layer as the most obvious exception.

Since we are interested in the overturning component of the circulation, it is helpful to decompose the transport as follows:

$$\begin{aligned} T(y, z) &= T_g(y, z) + T_{\text{Ek}}(y, z), \\ &= T_0(y) + T_c(y) + T_d(y, z) + T_{\text{Ek}}(y, z). \end{aligned} \quad (4)$$

Here,  $T_{\text{Ek}}(y, z)$  represents the zonal integral of all ageostrophic mass transports, which we assume are dominated by the wind-driven near-surface Ekman transport. This can be diagnosed from the wind stress alone, along with an assumption of its distribution within a near-surface layer. All other terms are therefore geostrophic and sum to give  $T_g(y, z)$ , and  $T_c$  (subscript  $c$  stands for compensation) is a depth-independent geostrophic term chosen to compensate  $T_{\text{Ek}}$  in a vertical integral. Thus,  $T_c + T_{\text{Ek}}$  represents an overturning circulation in which a near-surface southward flow is balanced by a geostrophic northward return flow for which the zonal integral is independent of depth. This is not supposed to be physically correct; the real return flow will be distributed over a range of depths. It is simply a mathematical device that conveniently allows us to separate out the part of the geostrophic flow for which the zonal integral depends on depth.

The term  $T_0$  is a constant, independent of depth, chosen such that  $T_0 H_{\text{max}} = Q$ , where  $H_{\text{max}}$  is the maximum ocean depth at that latitude and  $Q$  is the net northward mass transport across the latitude (a term often assumed to be zero, though it is not exactly so; in the Atlantic it includes the recirculation from the Pacific through the Bering Strait, as well as terms associated with mass sources and sinks, and the accumulation of mass north of the chosen latitude). In other words,  $T_0$  accounts for the net northward mass transport in a way that introduces no depth dependence, and is therefore irrelevant to the overturning component of the flow.

With these definitions, the depth-averaged geostrophic transport is  $T_0 + T_c$ , which leaves the term  $T_d(y, z)$  to represent departures of the zonally integrated geostrophic transport from its depth average (subscript  $d$  stands for depth dependent; by definition, the depth integral of  $T_d$  is zero). Taking the vertical derivative of (3), we find that

$$\frac{\partial}{\partial z} T_g(y, z) = \frac{\partial}{\partial z} T_d(y, z) = \frac{1}{f} \frac{\partial}{\partial z} [p_E(y, z) - p_W(y, z)]. \quad (5)$$

Given the constraint that the depth integral of  $T_d(y, z)$  is zero, this implies that all we need to determine this component of the overturning circulation is  $\partial/\partial z$  of the boundary pressure terms  $p_W$  and  $p_E$ . For the case in which the net northward transport  $T_0$  is known, this separation into depth-dependent and depth-independent components represents a means of determining the ‘‘reference level transport’’ in this analog of a thermal wind balance calculation. In the case of an ocean with vertical sidewalls, this is particularly simple as the hydrostatic balance equation can be used:

$$\frac{\partial p}{\partial z} = -\rho g. \quad (6)$$

When (as in reality) the ocean has sloping sidewalls, there are two approaches that can be taken. Use of the hydrostatic equation can be retained by defining a vertical-walled box within the ocean and calculating transports within this box, as is done within the RAPID-MOC array at 26°N (Rayner et al. 2011). In this case, there will be roughly triangular regions between the box and the sloping ocean walls that must be measured directly, with current meters, for example, to complete the integral across the entire basin. The alternative, which we focus on here, is to continue to integrate across the entire basin and to generalize the hydrostatic equation to work along lines that are not vertical. We do this by combining the hydrostatic Eq. (6) with the geostrophic relationship (2) to give an equation for the three-dimensional pressure gradient:

$$\nabla p = -\mathbf{k} \times (\rho f \mathbf{u}_g) - \mathbf{k} \rho g = \rho(\mathbf{i}v_g f - \mathbf{j}u_g f - \mathbf{k}g). \quad (7)$$

We can treat this relationship as a generalization of hydrostatic balance that allows the computation of pressure differences between any two points,  $c$  and  $a$ , rather than just points that are immediately above or below each other:

$$\begin{aligned} p_c - p_a &= - \int_a^c [\mathbf{k} \times (\rho f \mathbf{u}_g) + \mathbf{k} \rho g] \cdot d\mathbf{s}, \\ &= \int_a^c \rho f u_L ds - \int_{z_a}^{z_c} \rho g dz, \end{aligned} \quad (8)$$

where  $d\mathbf{s}$  is the three-dimensional differential vector along the path of the integral,  $ds$  is the infinitesimal horizontal distance along the line of the integral (in the case of a path at constant latitude it would be  $dx$ ), and  $u_L$  is the velocity directed to the left of that line (to the north, in the case of integrating in the positive  $x$  direction along a constant latitude line).

In the case where the integral is performed along (or just above) the seafloor, defined as  $z = -H(x, y)$ , we can write  $ds = -dz/H_s$  where  $H_s = \partial H/\partial s$ , so that (8) becomes

$$p_c - p_a = - \int_{z_a}^{z_c} \left( \frac{\rho f u_L}{H_s} + \rho g \right) dz. \quad (9)$$

This is a very simple principle. For a small separation between  $a$  and  $c$ , it can be thought of as using geostrophic balance to calculate (from the current) the horizontal pressure difference between  $a$  and  $c'$  (a point vertically above  $c$  but at the same depth as  $a$ ), followed by using hydrostatic balance to determine the pressure difference between  $c'$  and  $c$ .

Differentiating (9) with respect to  $z$  then gives

$$\frac{\partial p_b}{\partial z} = - \frac{\rho f u_L}{H_s} - \rho g, \quad (10)$$

which applies along a path on the seafloor (subscript  $b$  represents a value at the seafloor). This is the crucial relationship that allows us to infer gradients of boundary pressure from boundary measurements of density and current alone.

This is clearly a generalization of the hydrostatic relation for a sloping path. For the case in which the horizontal component of that path is zonal,  $u_L$  becomes  $v$  at the bottom and  $H_s$  becomes  $H_x$ , which, in combination with (5), gives

$$f \frac{\partial T}{\partial z} = g(\rho_W - \rho_E) + \left( \frac{\rho f v}{H_x} \right)_W - \left( \frac{\rho f v}{H_x} \right)_E. \quad (11)$$

For practical use, it is worth commenting that the density that appears in the hydrostatic part of (10) ( $\rho g$ ) and related equations can be replaced by a density anomaly [i.e., difference of density relative to a reference vertical profile,  $\rho' = \rho - \rho_r(z)$ ] as long as pressure is to be considered as the difference from the corresponding hydrostatic reference profile [ $p' = p - p_r(z)$ ]. However, wherever the density appears multiplying velocity, it must at least approximate the full density. In the case of an ocean model that uses the Boussinesq approximation, setting density to a constant  $\rho_0$  in the momentum equation, then  $\rho_0$  should be used to multiply velocity wherever the combination  $\rho u$ ,  $\rho v$ , or  $\rho w$  occurs: in the horizontal momentum balance and in (1), the definition of  $T$ . With such a convention, it becomes reasonable to separate the total  $z$ -dependent transport into contributions associated with density anomaly and current values at the eastern and western boundaries independently. Thus,  $T_d = T_E + T_W$ , and we can write

$$\begin{aligned} f T_E(y, z) &= p'_E(y, z) + C_E(y), \\ f T_W(y, z) &= -p'_W(y, z) + C_W(y), \end{aligned} \quad (12)$$

where  $C_E$  and  $C_W$  are constants at each latitude chosen, so that  $T_E$  and  $T_W$  each integrate to zero over the ocean depth, ensuring that each represents an overturning. With that constraint, any constant in the definition of the reference pressure profile becomes irrelevant, so all that needs to be specified is a reference density profile, which implies the pressure (apart from a constant) via hydrostatic balance. For present purposes we will, in concept, assume a time-independent reference density based on an average taken over an area of deep water toward the eastern side of the ocean basin, though this could in principle be a time-dependent profile (in practice, as we are here only looking at departures from a time average, the assumed reference profile plays no role). With this assumption, we can allocate components of the overturning circulation to the western and eastern boundaries separately, although this separation does not imply that the flows contributing to the transport must be concentrated near either boundary. Accompanying this decomposition, we must use the correspondingly modified version of the generalized hydrostatic equation:

$$\frac{\partial p'_b}{\partial z} = - \frac{\rho f u_L}{H_s} - \rho' g. \quad (13)$$

This modified form of (10) is the form we will use for calculations in section 4.

The relative importance of the velocity and density terms in (13) clearly depends on how steep the slope is, as the relationship reverts to hydrostatic balance when

the path becomes vertical and  $H_s$  becomes infinite. As an indication of the size of current needed, consider a circulation in which  $T_d$  (the depth-dependent part of the zonally integrated geostrophic northward mass transport) is constant above 500-m depth and then reduces linearly from a northward value  $T_s = 10^6 \text{ kg m}^{-1} \text{ s}^{-1}$  [approximately equivalent to 1 Sv ( $1 \text{ Sv} \equiv 10^6 \text{ m}^3 \text{ s}^{-1}$ ) per kilometer of depth] to 0, over 1000 m of depth. This gives a net northward transport above 1500 m of approximately 1 Sv and, below 500 m,  $T_z = \partial T_d / \partial z = 1000 \text{ kg m}^{-2} \text{ s}^{-1}$ . Assuming this is entirely due to the velocity term on the western boundary, rather than the density, this requires a bottom current given by  $v = H_x T_z / \rho$ , which for  $\rho = 1000 \text{ kg m}^{-3}$  leads to  $v = 1.0 \text{ m s}^{-1} \times H_x$ , meaning that a 1-Sv overturning would require  $10 \text{ cm s}^{-1}$  bottom currents on a slope of 0.1, or  $1 \text{ cm s}^{-1}$  on a slope of 0.01. For reference, the continental slope at the RS Line has a slope of about 0.05, reducing to 0.01 at the foot of the slope (Fig. 1). There is no practical difficulty in measuring currents to this accuracy; the only questions are whether they can be measured with sufficient spatial resolution, and whether the measured currents are sufficiently close to geostrophic for (13) to be used.

In comparison, in the case of the RAPID-MOC array at  $26^\circ\text{N}$ , the eastern continental slope is rather gentle, with a typical slope of only about 0.02, and less below about 3000 m. However, the western continental slope is extremely steep with an average slope between 1500 and 4000 m depths of about 0.35, and significantly steeper over some depth ranges (Rayner et al. 2011), reducing the relative contribution of currents to the boundary pressure gradient. In fact the WB2 mooring, in almost 4000-m depth, is only about 7 km horizontally from the 1500-m depth contour. The MOC calculation at  $26^\circ\text{N}$ , which relies on performing a thermal wind calculation for an interior boxlike ocean and then measuring currents to the west of that box, is effectively the same as calculating the vertical gradient of boundary pressure from the hydrostatic pressure gradient at WB2, extended to the western boundary using horizontal pressure gradients inferred from the currents. Seen purely from the point of view of determining the Eulerian MOC, parts of the  $26^\circ\text{N}$  array are thus redundant. From a wider perspective, these redundant parts add information about the local current structure and water mass properties, and they can improve the calculation of heat and buoyancy fluxes by accounting for correlations between currents and departures of temperature and density contours from the horizontal. The lack of current measurements on the gently sloping eastern boundary array calls into question the determination of the eastern boundary contribution to

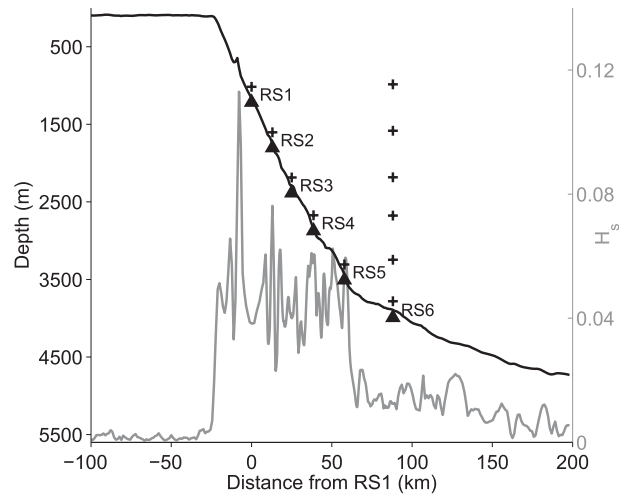


FIG. 1. Depth (black) and slope magnitude  $H_s$  (gray) as a function of distance along a great-circle arc aligned with the RS Line, using version 13.1 of the Smith and Sandwell (1997) topography dataset, at 1-min resolution. Black triangles show the positions of the BPRs at RS1–RS6, and pluses show the positions of MicroCATs. ADCPs are between the BPR and the (lowest) MicroCAT on each mooring.

total MOC variability on time scales for which currents contribute to this, although the eastern contribution is generally expected to be smaller than the western contribution.

The accuracy required of density measurements is given by assuming that the same vertical pressure gradient that was assumed above to result from currents instead results from the density anomaly in (13), that is,  $1000 \text{ kg m}^{-2} \text{ s}^{-1} = \rho' g / f$ . Taking  $g / f = 10^5 \text{ m s}^{-1}$  (which, coincidentally, is exactly true at a latitude lying within the RS Line) leads to an equivalent accuracy requirement for  $\rho'$  of  $0.01 \text{ kg m}^{-3}$ . This level of accuracy is attainable, although very careful calibration is needed to improve substantially upon this level. Thus, for slopes steeper than about 0.01, it is likely to be the accuracy of the density measurement that is the limiting factor if significant density variations occur and spatial sampling is sufficient.

Note that the presence of currents as well as density in (13) means that there is no need for the flow to have a vertical shear of the current in order to produce a vertical shear in the zonally integrated transport  $T$ . This is simple to understand: consider an ocean basin that is 4 km deep everywhere except in a region near the western boundary, where it is 1 km deep. If a depth-independent flow is to the north in the shallow region and to the south in the deep region (compensating each other so that there is no net northward mass transport), then  $T$  must be to the south at any depth below 1 km and, because it must integrate to zero, must be to the north at depths above that. There is therefore an overturning circulation with no vertical shear in the velocity.

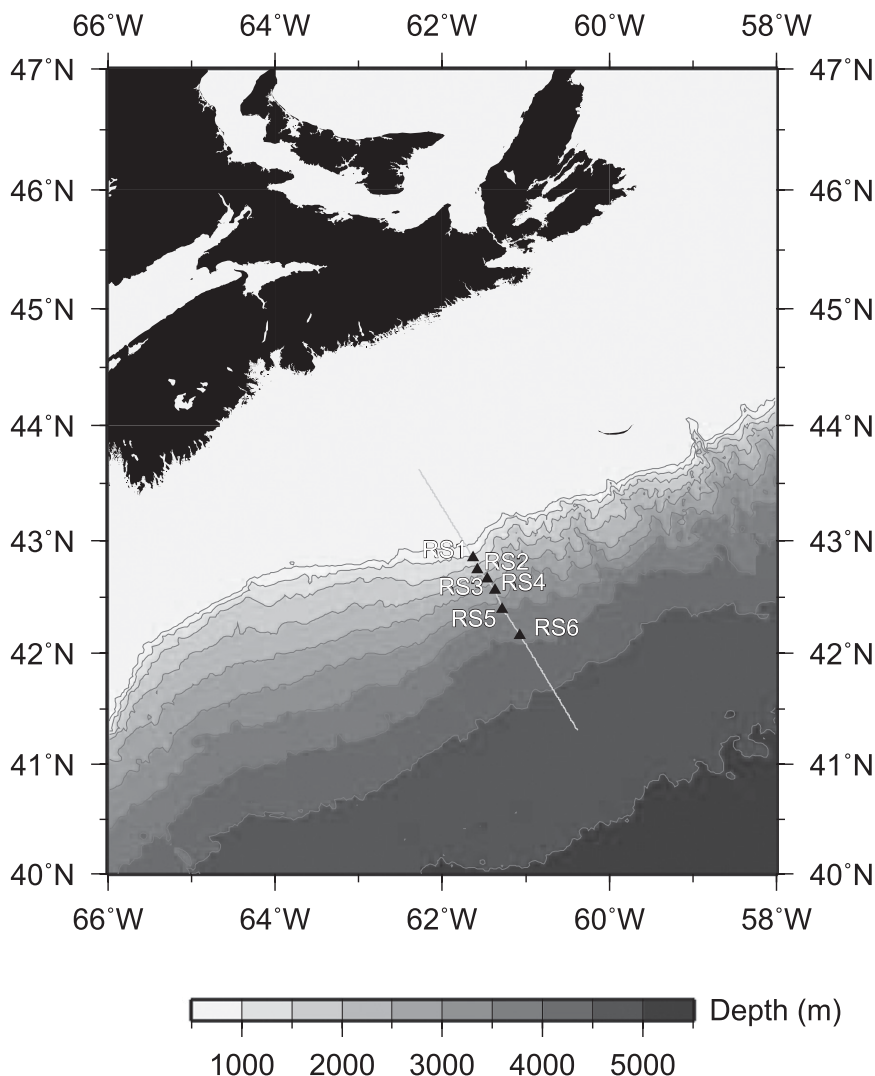


FIG. 2. The geography of the RS Line, showing the position of instruments (black triangles), together with depth contours every 500 m from version 13.1 of the Smith and Sandwell (1997) topography dataset, at 1-min resolution.

With this in mind, it clearly does not make sense to refer to  $T_d$  as a baroclinic transport and  $T_0$  and  $T_c$  as barotropic, although  $T_d$  has no depth integral and  $T_0$  and  $T_c$  have no depth dependence. For that reason, we refer to  $T_d$  as an overturning transport. Other concepts familiar from thermal wind calculations remain valid, such as the concept of a flow (in this case a zonally integrated transport) measured relative to an assumed depth of no (zonally integrated) motion, but such a flow need not be baroclinic in nature.

### 3. Measurements on the RAPID-Scotian Line

The fourth deployment of the WAVE experiment (the first with a suite of current and density measurements)

under the National Environment Research Council (NERC)-funded RAPID-Will the Atlantic Thermohaline Circulation Halt? (WATCH) program took place on 2 and 3 October 2008, during the Canadian Coast Guard Ship (CCGS) *Hudson* expedition 2008-037, under a collaboration between the U.K. National Oceanography Centre and the Canadian Bedford Institute of Oceanography. The RS array, consisting of five short moorings (RS1-RS5) and one tall mooring (RS6), was deployed across the Scotian continental slope between approximately 1100- and 3900-m water depth (Figs. 1 and 2; Table 1). Each short mooring (approximately 100-m length) was equipped with a Sea-Bird Electronics (SBE) 53 bottom pressure recorder (BPR) on its anchor, an upward-oriented 120-m nominal range Teledyne RD

TABLE 1. Summary of the RS Line deployment. In the water depth column, the figures in parentheses are linearly interpolated from Smith and Sandwell (1997) seafloor topography data at 1-min resolution (version 13.1), but smoothed with a 20-point 2D Gaussian window.

Mooring site	Location	Measured water depth (m)	BPR and $\mu$ CAT records (days)	ADCP velocity records (days)
RS1	42°50.95'N, 61°37.85'W	1114 (1176)	359.1	359.5
RS2	42°44.26'N, 61°34.61'W	1701 (1771)	359.3	269.2
RS3	42°39.50'N, 61°27.70'W	2290 (2293)	359.7	360
RS4	42°33.35'N, 61°22.14'W	2784 (2766)	360.5	310.3
RS5	42°23.56'N, 61°16.57'W	3427 (3427)	361.2	—
RS6	42°09.81'N, 61°04.22'W	3882 (3916)	361.5	283.1

Instruments Workhorse 300-kHz acoustic Doppler current profiler (ADCP) mounted 50 m above the anchor and, a further 50 m above, a SBE37 (MicroCAT) temperature–conductivity–pressure recorder. The tall mooring RS6 (3000-m length) had the same configuration at its bottom but included five additional MicroCATs mounted at approximately the same depths as the MicroCATs on the short moorings up the slope.

From the nearby Line B, described in Elipot et al. (2013), earlier near-bottom temperature measurements had shown that temperature variations are highly coherent throughout the range 100–500 m above the bottom, but temperatures at the bottom are somewhat different. This implies a bottom boundary layer of less than 100-m thickness, consistent with the more general findings of Lozovatsky and Shapovalov (2012).

Recovery and redeployment of the moorings took place during the Hudson expedition 2009–048, between 26 and 30 September 2009. All instruments returned data except the ADCP at RS5, which was flooded. Table 1 provides a summary of location, water depth, and instrumental record length of each mooring.

With these measurements, we have the information necessary to assess whether downslope pressure gradients can be reconstructed accurately from current and density measurements as given by (13). On the left-hand side of this equation, the pressure differences are obtained from the BPR data. Such data always suffer from drifts (Watts and Kontoyiannis 1990) and the impossibility of determining absolute pressure and depth to the subcentimeter accuracy required. In addition, the assumption of geostrophic balance cannot be expected to hold at periods shorter than about a day. For these reasons, we focus on versions of the time series that have been filtered to pass periods between 1 and 50 days (from spectral analysis of pressure difference time series with and without removal of drifts, the effect of drift dominates at periods longer than about 50 days). As we show below, the resulting time series compare well with the reconstructions from velocity and density data.

#### a. Bottom pressure estimates from BPR measurements

The manufacturer's calibrations were applied to the BPR data, which were sampled as 5-min averages every 20 min. High-frequency tides were removed by least squares fitting of 97 tidal components with periods of 28.0062 h (2Q1) and shorter. There is too much power near the periods of the fortnightly and monthly tides for a reliable estimate of these to be made from the data (expected amplitudes of these tides are below 1 hPa), so these tides remain in the records but are not expected to change by much across the array. Pressure differences at these longer periods should in any case be close to geostrophic balance and should therefore also appear in the currents.

Intercomparison of the tidal residuals (Fig. 3) showed that five of the six datasets had drifts compatible with the expected exponential-plus-linear function of time as described by Watts and Kontoyiannis (1990). The exception was RS3, which, in comparison with the average of RS2 and RS4, showed four short periods of disruption, producing steps in the record, each of which appeared to initiate a new exponential adjustment phase with approximately the same amplitude and time constant. If the steps had resulted from a movement of the instrument, then we would not expect such exponential adjustments, given that the steps are only of order 10–20 hPa, smaller than the tidal amplitude (we cannot use the density or current measurements to check for such a small instrument movement, although it is clear from the current measurements that there was no significant rotation of the instrument). The comparison in section 4 shows that the jumps and exponentials cannot be genuine signals. Thus, we assume the disturbances to be instrumental errors perhaps associated with anomalous behavior of the quartz crystal. Steps plus exponentials were added following each event, the latter each having an amplitude of 1.5 hPa and time constant of 200 time steps, or 66 h and 40 min. While this procedure brought the variability at RS3 into line with the other

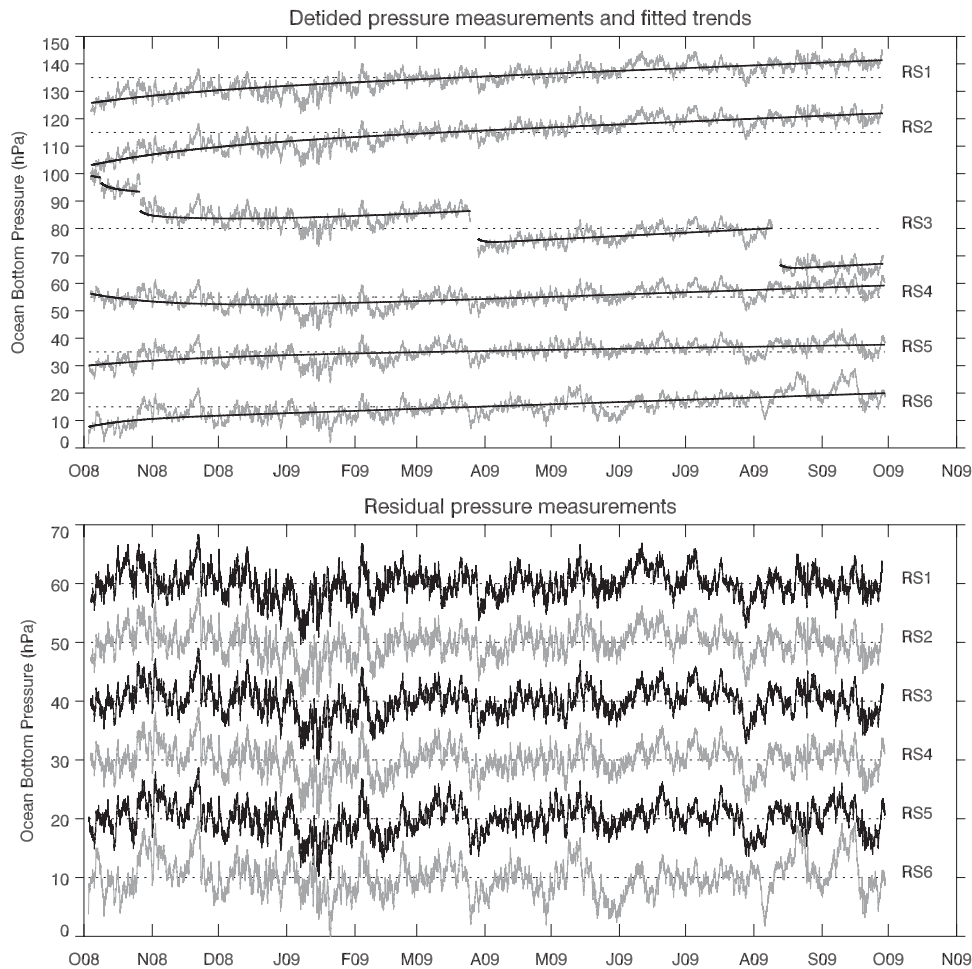


FIG. 3. Bottom pressure anomalies from the time mean, after subtraction of diurnal and higher-frequency tides. (top) Data before detrending together with the fitted trend functions. (bottom) Residuals after detrending. Arbitrary vertical offsets have been applied for display purposes (dotted lines).

records, the resulting time series should be treated with caution.

Following the special treatment of RS3, a composite record was formed from the average of all six time series and a linear trend removed from the composite. Exponential-plus-linear trends were then fitted to the differences of each record from the composite record. The initial (detided) time series, overall fitted trends, and final residuals are plotted in Fig. 3. The residual time series are clearly dominated by a highly coherent mode, although additional variability is also apparent at RS6. This is also clear from the standard deviations, which increase gradually from 2.46 hPa at RS1 to 2.57 hPa at RS5, and then jump to 3.01 hPa at RS6. In an attempt to reduce trends from clock drift, a reference clock comparison was available every 7 days, but the observed trend amplitude was typically about 10 times larger than could be accounted for from this source (and the jumps

in RS3 were not explained by the comparison), so information from the reference clock was not used further.

Figure 4 shows the difference between neighboring pairs of residual pressures. The differences clearly have a spectrum that is different from the full pressure, and also show a degree of coherence between depths, with RS6 once again standing out as introducing extra variability (with some also at RS5). These time series have standard deviations of between 0.67 and 0.9 hPa except for RS6–RS5, which has a standard deviation of 2.1 hPa.

#### b. Velocity estimates from ADCP measurements

The ADCPs were configured to have hourly sampling, and their depth bins were centered at 4-m range intervals, with the first bin centered on 6.1 m and the 30th bin centered on 122.1 m above the instrument. Hourly current directions in each bin were rotated into an Earth-fixed

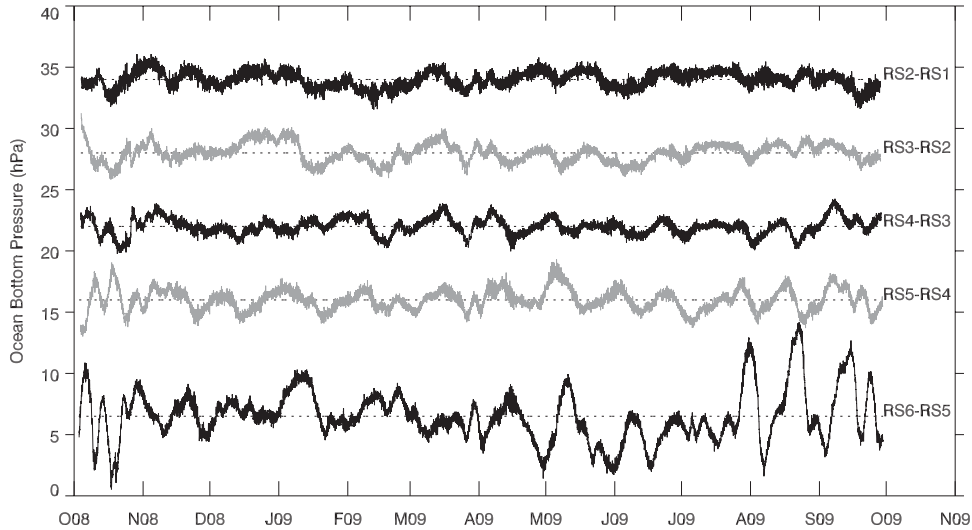


FIG. 4. Differences between neighboring pairs of bottom pressure residuals. Arbitrary mean values have been added for display purposes (dotted lines).

coordinate system using the magnetic compass of the instrument, corrected for the local magnetic declination. A time-dependent magnetic declination correction was obtained from the magnetic field calculator of the U.S. National Geophysical Data Center (approximately  $-18^\circ$  at these locations and times). The data from the first bin of each ADCP were degraded and hence discarded. The data were processed using the Teledyne RD Instruments processing software, with standard error thresholds used to determine which bins were returning good data. The usable range varied with time and mooring, with the last usable bin being bin 30 for RS1, between 23 and 30 for RS2, between 17 and 30 for RS3, and between 11 and 29 for both RS4 and RS6.

An inspection of the velocity time series in each bin revealed that currents are very strongly correlated in the vertical, and almost independent of depth between bins 2 and 8 or 9. For a few bins either side of the depth of the MicroCAT instrument mounted on each mooring (approximately 50 m above the ADCP), velocities appeared to be biased low, but beyond the MicroCAT an increase in velocity was seen. To avoid any question of tuning the data to match the pressure observations, we simply considered the velocity averaged over all bins considered to be good at any time. Tests using an alternative average over bins 2–8 and 2–9 produced insignificant differences in the pressure reconstructions reported in section 4.

The principal components of the resulting velocity time series at each mooring are plotted in Fig. 5, with the corresponding variance ellipses plotted in Fig. 6. For display purpose only, these series have been filtered by a third-order Chebyshev low-pass filter with 0.5-dB

peak-to-peak ripple in the passband, with a frequency cutoff of 1 cpd.

Generally, the flow across depth contours is suppressed compared to that along the contours, especially at longer periods. Like the pressure differences, the along-slope flow fluctuations are coherent from one site to the next, but greater variability is seen at the deepest site (RS6).

### c. Density estimates and their errors

The MicroCAT datasets (with sampling every 10 min) are of very high quality for temperature and conductivity but exhibit some significant drifts and offsets for their pressure records, which can be important for the computation of in situ density. The onboard calibration procedure described in Kanzow et al. (2006) was applied to each instrument, during both deployment and recovery cruises. This process involves taking collocated measurements with both MicroCATs and shipboard CTD, which were in turn carefully calibrated against bottle samples by Igor Yashayaev (Bedford Institute of Oceanography).

Our best values, used here, use calibration coefficients interpolated linearly in time between the values determined at deployment and recovery of the instruments. The root-mean-square differences between the pre- and post-calibrated temperature, conductivity, and pressure of the MicroCATs are on average  $1.1 \times 10^{-3}$  K,  $2.1 \times 10^{-4}$  S  $m^{-1}$ , and 4.5 dbar. These values are consistent with the expected errors provided by the manufacturer. Salinity was computed from the calibrated temperature, conductivity, and pressure, and then despiked

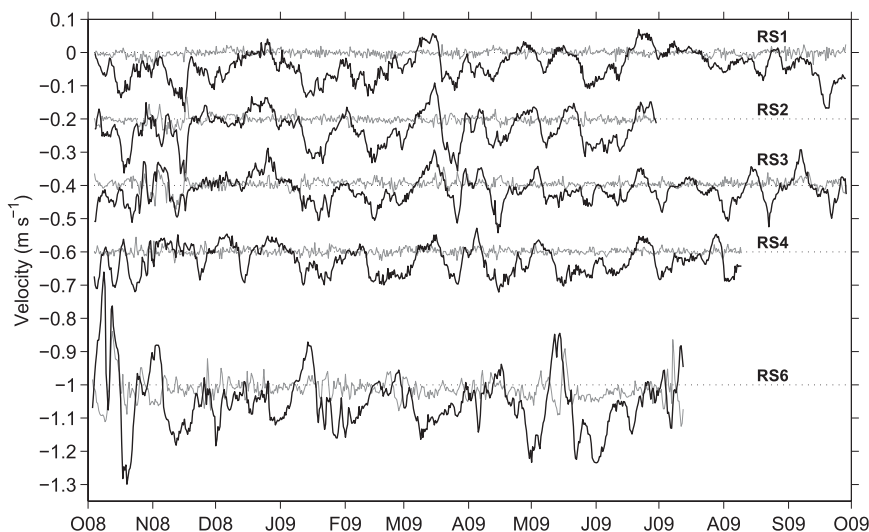


FIG. 5. Vertically averaged near-bottom velocity records lowpassed below 1 cpd. Black curves: first principal components at each site. Gray curves: second principal components. The orientations of the principal components at each site are shown in Fig. 6. The curves for RS2, RS3, RS4, and RS6 are offset by  $-0.2$ ,  $-0.4$ ,  $-0.6$ , and  $-1$   $\text{m s}^{-1}$ , respectively.

based on a threshold value of the second-order time derivative.

Roughly (to better than a factor of 2 depending on water properties), errors of the size noted above imply a salinity-induced density error of  $0.004 \text{ kg m}^{-3}$ , and hence a pressure error of  $40 \text{ Pa km}^{-1}$  and a temperature-induced error of  $2 \text{ Pa km}^{-1}$ . The pressure uncertainty of  $45 \text{ kPa}$  (equivalent to approximately  $4.5\text{-m}$  uncertainty in depth) produces a density error of about  $0.02 \text{ kg m}^{-3}$ , which would give a larger error of about  $200 \text{ Pa km}^{-1}$ . However, that is an overestimate of the effect of pressure errors in our calculation. We are only concerned with the density difference between two points at the same, constant depth. Excluding tidal variability, Fig. 3 shows that such points will always be at the same pressure to within  $2 \text{ kPa}$  or so, about a factor of 20 smaller than the  $45 \text{ kPa}$  uncertainty in pressure measured on the MicroCAT. Thus, the relevant pressure-related uncertainty is about 20 times smaller than  $200 \text{ Pa km}^{-1}$ , giving  $10 \text{ Pa km}^{-1}$ . We simply have to ensure that density is always calculated as the difference from a reference density calculated at the same pressure. To this end, the densities we use are calculated at a constant pressure for each site, corresponding to the time average of the pressure measured by the BPR.

Consistent with the above-mentioned error estimates, the difference in densities calculated using the pre-calibration temperature and salinity and our final product (both at the same standard pressure) has a standard deviation of between  $0.0011$  and  $0.0055 \text{ kg m}^{-3}$  for the six sites. The calibrated data should be better, and in an

attempt to assess how much better, we have calculated differences between densities using either the two different calibrations (predeployment and postdeployment) and our final product, which interpolates in time between the two calibrations. These give standard deviations between  $0.0015$  and  $0.0026 \text{ kg m}^{-3}$ , leading to pressure errors of  $15\text{--}26 \text{ Pa km}^{-1}$ . Smaller errors would be appropriate if the linear drift in calibration is a good model, but it is worth noting that these errors (dominated by the salinity term) are not completely negligible in comparison to the  $100 \text{ Pa km}^{-1}$  signal produced in our example case of  $1\text{-Sv}$  overturning. Exactly the same errors are incurred in a conventional thermal wind calculation using a vertical mooring.

Figure 7 shows the 10-min interval time series of in situ density anomalies. For display purposes, low-passed versions of each time series, using the same filter as for the velocity time series, are also shown. For comparison, the in situ density anomalies estimated from the RS6 mooring data at similar pressure levels are also shown in Fig. 7b. Note the substantial differences between these time series and the near-bottom time series at the equivalent depths, especially for the shallower data.

#### d. Expected errors due to the geostrophic assumption

The development so far has been based on the assumption that the horizontal flow is geostrophic. In the bottom boundary layer, this can be upset by turbulent viscosity but, as noted above, we believe our measurements to be outside the boundary layer. However, there are other ageostrophic terms that can upset the assumed

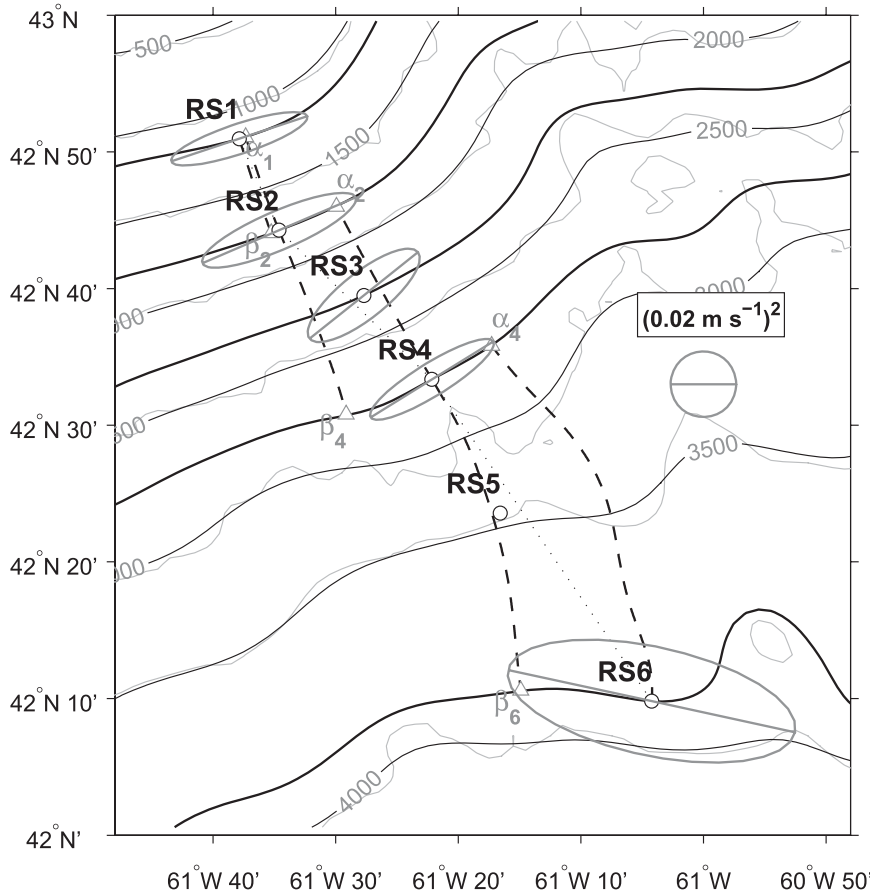


FIG. 6. Gray lines: depth contours at 500-m intervals from Smith and Sandwell (1997) topography version 13.1. Thin black lines: same contours smoothed by a two-dimensional Gaussian window of 20' radius. Black lines: smoothed depth contours at the depths of the moorings RS1, RS2, RS3, RS4, and RS6. The path RS1 to  $\beta_2$  (dashed line) is the steepest descent from RS1 to the depth contour of RS2. The path RS2 to  $\alpha_1$  is the steepest ascent from RS2 to the depth contour of RS1, and so on (see text). Variance ellipses and their major axes are plotted for the vertically averaged velocity record lowpassed below 1 cps.

balance. The size of these can be assessed by extending (2) to include time-dependent and nonlinear terms:

$$\frac{\partial \mathbf{u}}{\partial t} + (f + \zeta) \mathbf{k} \times \mathbf{u} + w \frac{\partial \mathbf{u}}{\partial z} = - \left[ \frac{\nabla_h p}{\rho} + \frac{\nabla_h (\mathbf{u} \cdot \mathbf{u})}{2} \right], \quad (14)$$

where  $\zeta$  is the vertical component of the relative vorticity.

The relative size of the ageostrophic terms can be assessed by comparing them with the geostrophic terms of size  $f\mathbf{u}$  and  $(\nabla_h p)/\rho$ . The first, time-dependent term is smaller than  $f\mathbf{u}$  by a factor  $\omega/f$ , where  $\omega$  is the angular frequency of the oscillations in velocity. At the latitude of the array, this ratio is 1 at a period of 0.73 days, reducing to 0.1 at 7.3 days, and so on, so we can expect strong deviations from geostrophy at periods of a few days and shorter.

The size of the first nonlinear term can be assessed from the ratio  $\zeta/f$ , with a scale for  $\zeta$  given by  $V/L$ , where

$V$  is a change in along-slope velocity over a length scale  $L$ . From Fig. 5, a typical velocity is  $0.05 \text{ m s}^{-1}$  and a large velocity is  $0.1 \text{ m s}^{-1}$  except at RS5, where the extreme velocity reaches about 0.3 and  $0.1 \text{ m s}^{-1}$  might be considered typical. The horizontal separation between measurements is typically about 10 km, and the coherence between measurements at different depths means that the relevant velocity difference  $V$  will be smaller than the total velocity. Thus, taking  $V = 0.05 \text{ m s}^{-1}$ ,  $L = 10 \text{ km}$ , and  $f = 10^{-4} \text{ s}^{-1}$ , we obtain a ratio  $\zeta/f = 0.05$ , with slightly larger values expected at RS6, meaning the flow should be comfortably within 10% of geostrophy except perhaps at the deepest station.

The fractional disturbance to geostrophy from the second nonlinear term is  $wu_z/fv$ , where  $u_z = \partial u/\partial z$  and  $u$  is the downslope velocity component. We can estimate

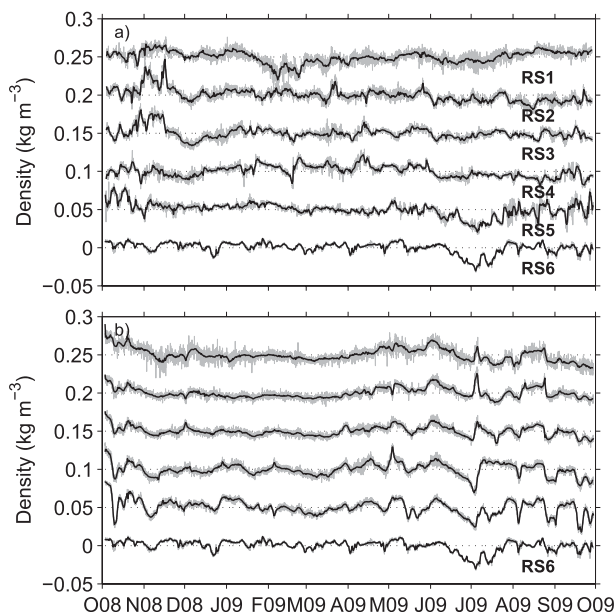


FIG. 7. In situ density anomalies calculated from MicroCAT records (a) at moorings RS1–RS6 and (b) from instruments on tall mooring RS6. Arbitrary offsets of  $0.05 \text{ kg m}^{-3}$  between curves are applied for legibility. The bottom curve in (a) is repeated as the bottom curve in (b). Data are shown every 10 min (gray), and after applying a 1 cycle per day (cpd) low-pass filter (black).

the size of  $w$  from  $u \times s$ , where  $s$  is the slope (about 0.05) and make an overestimate of  $u_z$  as  $u/h$  with  $h = 50 \text{ m}$  [this assumes that the vertical shear produces an order (1) change to the flow over 50 m, larger than we see in the ADCP data, which usually have rather little shear in the first 50 m]. Using these estimates leads to  $wu_z/fv < u^2s/fvh$  and writing  $u = \beta v$  and then substituting numerical values for  $s$ ,  $f$ , and  $h$  gives  $wu_z/fv < 10\beta^2v$  with  $v$  in meters per second. With along-slope velocities typically more than 3 times larger than cross-slope velocities (Figs. 5 and 6), this results in  $wu_z/fv < v \text{ (m s}^{-1}\text{)}$ . This gives an upper bound on the effect of the second nonlinear term, which is similar in size to the first.

The size of the third nonlinear term (on the right-hand side of the equation) is best expressed by comparing it directly with a pressure signal. The size of the perturbation to the pressure is thus given by  $\rho U^2/2$ , where  $U$  now is the total velocity. Choosing  $U = 0.1 \text{ m s}^{-1}$ , this gives a value of 5 Pa, equivalent to 0.5 mm of water. This is an upper limit for RS1–RS4, and the quadratic dependence on  $U$  means that the effect will usually be substantially smaller. At RS6, the occasional extreme value of about  $0.3 \text{ m s}^{-1}$  leads to a 10 times larger perturbation of around 50 Pa, or 5 mm of water.

Taken together, these scalings suggest that the dynamical balance we observe should be within 10% of geostrophic at periods longer than about 14 days, with

perhaps larger departures up to about 5 mm of water (50 Pa) at the deepest site. This is an assessment of the dynamical error, independent of instrumental or sampling errors.

#### 4. Test of the stepping method

The generalized hydrostatic relationship (13) allows us to use measurements of density and currents to calculate pressure differences between two sites on the continental slope. We refer to the use of this equation as the “stepping method.” With the reality of discrete measurements at six sites, this allows us to calculate five steps in pressure, and questions arise about how best to perform these discrete steps. These are addressed in the appendix, in which we derive three different methods. Method 1, using Eq. (A10), effectively assumes that currents should be linearly interpolated between measurement sites. Method 2, using Eq. (A12), assumes that the flow is strongly steered by topography, and the dominant interpolation error results from the fact that the topographic gradient is not constant between measurements. Method 2e, using Eq. (A16), is an extension of method 2 that also accounts for cross-slope flows on the assumption that these are not a source of noise for the geostrophic calculation.

Density and pressure data are available for all sites, but no currents are available from RS5 (Table 1). To be able to use the stepping method at all depths, we calculated a synthetic velocity time series for RS5 based on a linear combination of lagged velocities at RS4 and RS6, with lags and coefficients chosen so as to produce the best agreement between the RS4 and RS5 directly measured pressure difference time series and that produced by the stepping method. Thus,

$$v_5(t) = a_4 v_4(t - \tau_4) + a_6 v_6(t - \tau_6), \quad (15)$$

where the optimal parameters for method (1, 2) are  $a_4 = (0.58, 0.60)$ ,  $a_6 = (0.26, 0.24)$ ,  $\tau_4 = (2.45, 2.58)$  days, and  $\tau_6 = (-3.85, -3.82)$  days, implying a signal that propagates down the slope with time.

This is the only case for which any tuning has been applied. A degree of confidence in the reconstructed velocity is obtained from the fact that it does not noticeably degrade the fit for the independent RS5–RS6 step, and in fact improves the skill from 0.45 to 0.58 in the case of method 1, as compared to a reconstruction using weighted RS6 velocity only. We define skill as the fraction of variance of the measured pressure difference explained by the stepping method, without any scaling applied. Mathematically, skill is defined as

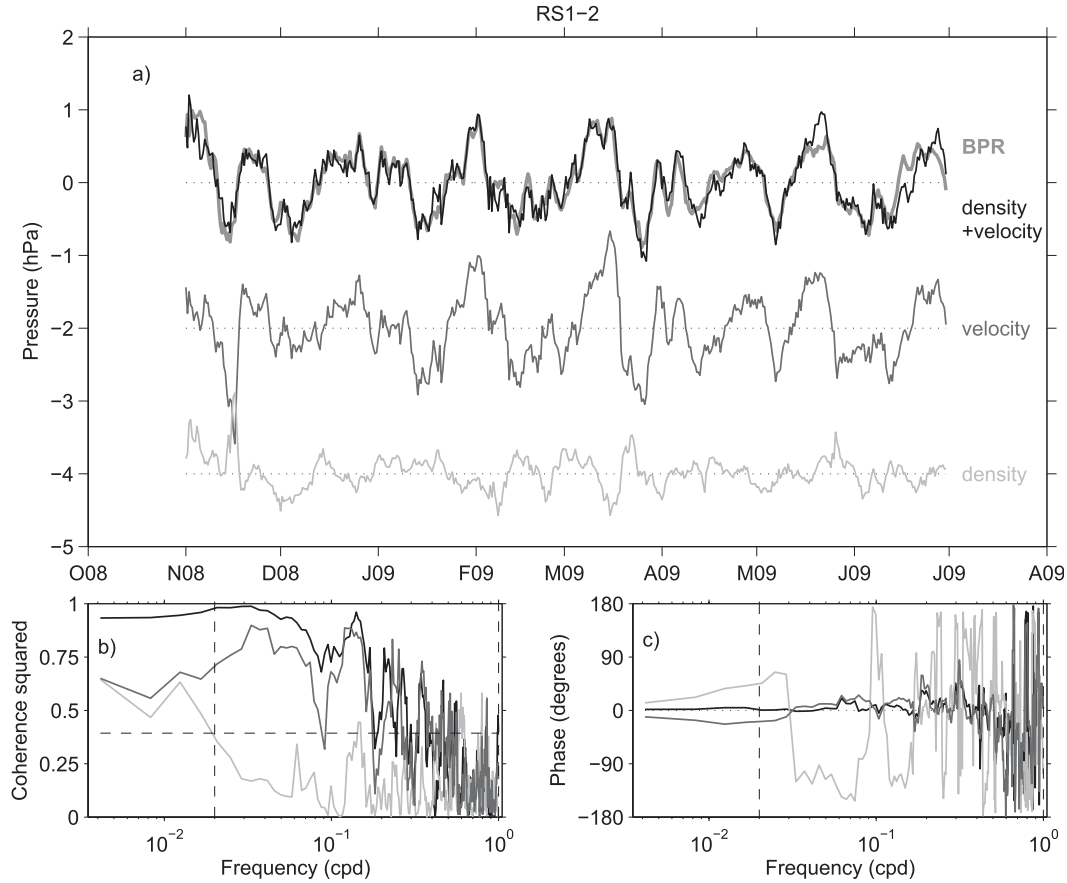


FIG. 8. (a) Pressure anomaly differences RS2 – RS1 as measured by BPR (thick gray) and as reconstructed by method 1 (black; see the appendix). The individual contributions to the reconstruction from velocity and density are shown with offsets. (b) Squared coherence, and (c) phase of cross spectra of the different components of the reconstructed pressure difference vs that directly measured from BPRs. Shades of curves match those in (a). In (b), the horizontal dashed line indicates the 95% confidence level for coherence squared. In (a), the time series have been bandpass filtered between 1- and 50-day periods. The cutoff frequencies are marked as vertical dashed lines in (b) and (c).

$$1 - \langle (\delta p - \delta q)^2 \rangle / \langle \delta p^2 \rangle, \quad (16)$$

where  $\langle \cdot \rangle$  represents a time average;  $\delta p$  is the directly measured pressure difference between two sites, minus its time average; and  $\delta q$  is the pressure difference between two sites reconstructed from density and current measurements, minus its time average.

With this tuning for RS5 velocity, and the doubts discussed above for the RS3 OBP, that leaves us with two completely “clean” cases to test. The RS1–RS2 step has complete information, and we can also compare the RS2–RS4 pressure difference with the sum of the two steps, RS2 and RS3 and RS3 and RS4. For these steps, the directly measured pressure differences and reconstructions using method 1 are illustrated in Figs. 8 and 9. Note that we use the convention of plotting deeper minus shallower pressure and, for time series

plots and statistics quoted, we apply a 1–50-day bandpass filter because geostrophy can only hold at periods longer than the inertial period (0.74 days), and the power in the OBP drift correction becomes dominant at longer periods. We also ignore the first month of observations because of apparent remaining drifts in the BPR records, despite the detrending applied to the data.

Figures 8 and 9 tell us a number of things. The reconstruction is very good, particularly (as expected) at periods long compared to the inertial period. Both velocity and density contribute to the reconstruction, with the density contribution being smaller but increasing in relative size at longer periods (there is a noticeable improvement in phase agreement when the density contribution is included). There is a strong dip in the squared coherence at about 0.2 cpd (5-day period), and a weaker dip around 0.09 cpd (11-day period). The

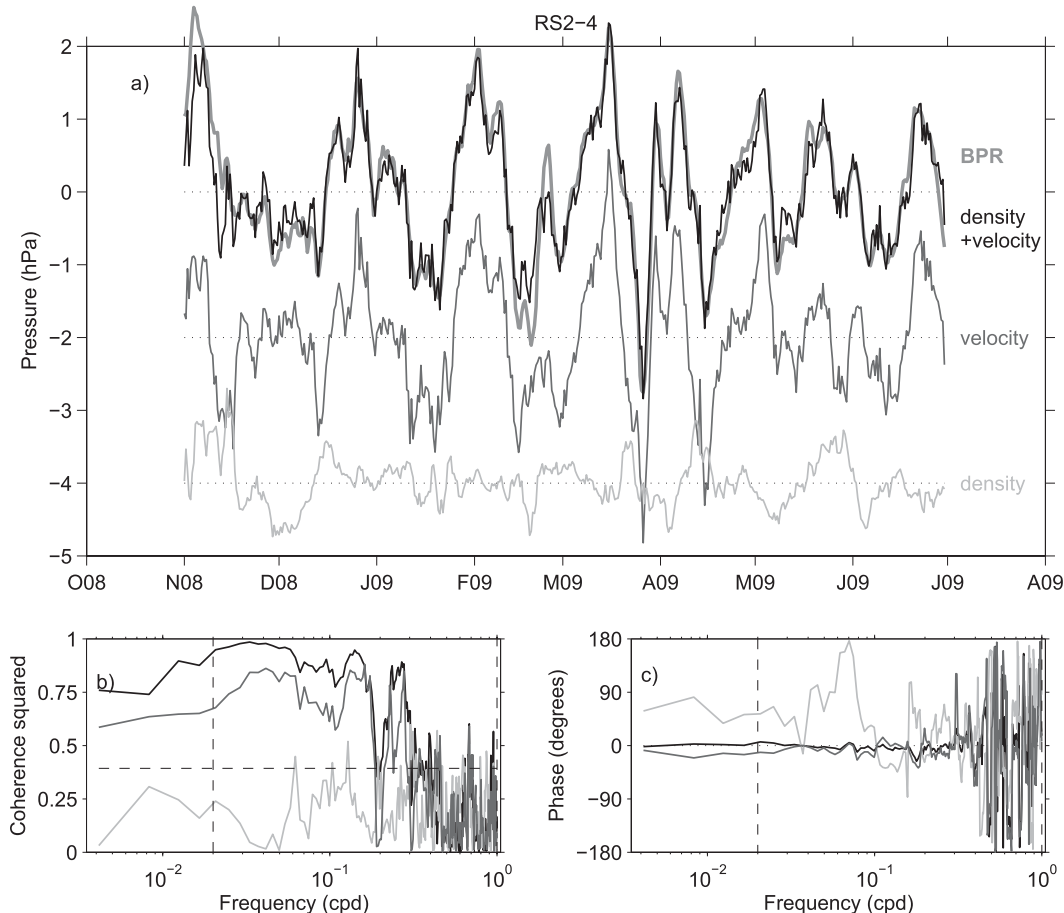


FIG. 9. As in Fig. 8, but for the pressure difference RS4 – RS2.

causes of these dips are not known, but they are seen for all pairs of sites (not shown) and suggest an ageostrophic mode of variability at these frequencies.

The quality of the reconstruction for all neighboring pairs of instruments is shown in Table 2. Errors are typically 20–30 Pa, except in the poorly sampled deepest region for which some velocity data are missing. In section 3c, we estimated a measurement error dominated by salinity calibration errors of about  $20 \text{ Pa km}^{-1}$ , which translates to 10 Pa over the approximately 500-m steps here. The reconstruction includes three further sources of error: sampling error, representation error, and errors in the BPR data. Sampling error relates to the spatial resolution of the measurements and the question of whether the necessary interpolation is adequate; representation error relates to the question of whether the pressure gradients are sufficiently close to geostrophic and hydrostatic balance with the measured current and density, respectively. The fact that the total error is comparable to the estimated measurement error shows that neither sampling nor representation

error is overwhelmingly large compared to measurement error.

Based on the skills and errors in Table 2, we cannot say whether method 1 or method 2 is better. Method 2e is systematically (though not significantly) worse than method 2 except at RS5 and RS6, where method 1 clearly does best. This reflects the fact that the measured velocities are highly correlated between neighboring sites, again suggesting that they are well resolved except at the deepest sites, where data are missing and where the variability in pressure differences rises rapidly between sites. As we saw in Fig. 4, extra variability is introduced below RS5, where the continental slope becomes less steep. This, coupled with the missing velocity data from RS5, results in a significantly degraded reconstruction at RS6.

It is also noteworthy that, although density alone accounts for only a small part of the variance (it actually has negative skill for RS1,2), addition of the density contribution to the velocity contribution typically increases the skill from about 0.6 to 0.8 (again, with the

TABLE 2. Skill [fraction of variance in directly measured pressure difference explained by reconstructions; see (16)] for reconstructions based on density only ( $\rho$  skill), velocity only ( $v$  skill), and density and velocity using method 1, method 2, and method 2e. The final column shows the residual standard error using the full reconstruction. Pairs for which data are complete with no known errors are marked in bold.

Pair	Method	$\rho$ skill	$v$ skill	Skill	Error (Pa)
<b>RS1,2</b>	1	-0.25	0.62	0.84	16.68
	2	-0.25	0.63	0.84	16.73
	2e			0.83	16.85
<b>RS2,4</b>	1	0.07	0.69	0.89	31.25
	2	0.07	0.69	0.90	30.42
	2e			0.89	31.83
RS2,3	1	0.04	0.55	0.76	27.40
	2	0.04	0.56	0.77	26.87
	2e			0.75	27.83
RS3,4	1	0.08	0.62	0.79	22.37
	2	0.08	0.60	0.78	22.95
	2e			0.76	23.82
RS4,5	1	0.12	0.62	0.68	36.13
	2	0.12	0.60	0.66	37.27
	2e			0.66	37.73
RS5,6	1	-0.02	0.59	0.58	76.84
	2	-0.02	0.35	0.39	92.79
	2e			0.45	87.61

exception of steps involving RS5, and higher for the cases excluding the dubious pressure record at RS3). Again, we see that density is making an important contribution, although the dominant signal is due to velocity.

The aim of the method is to determine pressure anomalies relative to a particular reference depth. Accordingly, the quantity of interest is the pressure difference relative to RS1, which is shown in Fig. 10. Table 3 lists, for method 1 and method 2, the skills and remaining errors for such pairs. Excluding the final step to RS6, the stepping method explains between 84% and 92% of the variance in each time series, with total error rising gradually with depth to about 50 Pa and jumping to about 100 Pa at RS6.

Using this pressure field to calculate  $T_w$ , the western contribution to the zonally integrated geostrophic transport from (12), and linearly interpolating these transports between measurement depths, we can integrate up the implied meridional transport below and relative to the depth of RS1, which results in standard deviations of total transport integrated between RS1 and (RS4, RS5, RS6) respectively of (0.98, 1.87, 2.56) Sv based on BPR data, and (0.91, 1.77, 2.50) Sv based on the stepping method. The corresponding difference time series have standard deviations of (0.32, 0.56, 0.82) Sv, and these numbers serve as error estimates for the transport determinations (data from October 2008 are not used in

determining these figures, as the initial transient in the BPR data remains significant over this period). Note that these transport measurements are, strictly speaking, mass transports measured in units of megatonnes per second ( $\text{Mt s}^{-1}$ ), equivalent to Sv for a density of  $1000 \text{ kg m}^{-3}$ . Using the true density changes the numbers by a few percent and adds a similarly sized depth dependence, which only serves to confuse interpretation as it is mass, not volume, that is the conserved quantity.

The above-mentioned figures are based on bandpass filtered time series, which pass the longest period of 50 days, as plotted in Fig. 10a. This long period limit was imposed by limitations of the BPR measurements, but those limitations do not apply to the stepping method, as density and velocity measurements suffer from much lower long period errors. Accordingly, in Fig. 10b we plot the same quantity, but with a low-pass filter applied that passes all periods longer than 1 day. The gray line in this figure shows the density contribution to these total pressure time series. Standard deviations of transports integrated from RS1 to (RS4, RS5, RS6) are increased to (1.28, 2.45, 3.49) Sv, with the density contribution to transport producing standard deviations of (0.81, 1.45, 1.99) Sv.

The density contribution is again seen to contribute significantly, especially at the longest time scales, although the contribution resulting from currents clearly dominates. Most importantly, repeated deployments of the array, which would introduce unknown offsets in the directly measured pressure time series, will introduce much smaller calibration errors via the stepping method. This means that it will be possible using later deployments to produce a time series capable of resolving interannual variability in the transports.

Finally, we revisit the question of trends in the BPR data. The detrending described in section 3a used only BPR data, in order to ensure that comparisons were between independent datasets. However, once the stepping method is accepted, it provides a means to improve the choice of detrending. Given that the stepping method only provides a measure of pressure differences, it clearly cannot resolve separate linear trends for each BPR, as the same trend could be added to each time series without appearing in the differences. The situation is, in principle, different for the exponential part of the trend: if different exponentials have different time constants, then a fit of  $N$  exponentials (one for each pressure time series) to  $N - 1$  time series of pressure differences could be possible. In practice, however, we find that such a simultaneous fit is unstable and produces very little reduction of residuals beyond the simpler method we describe here.

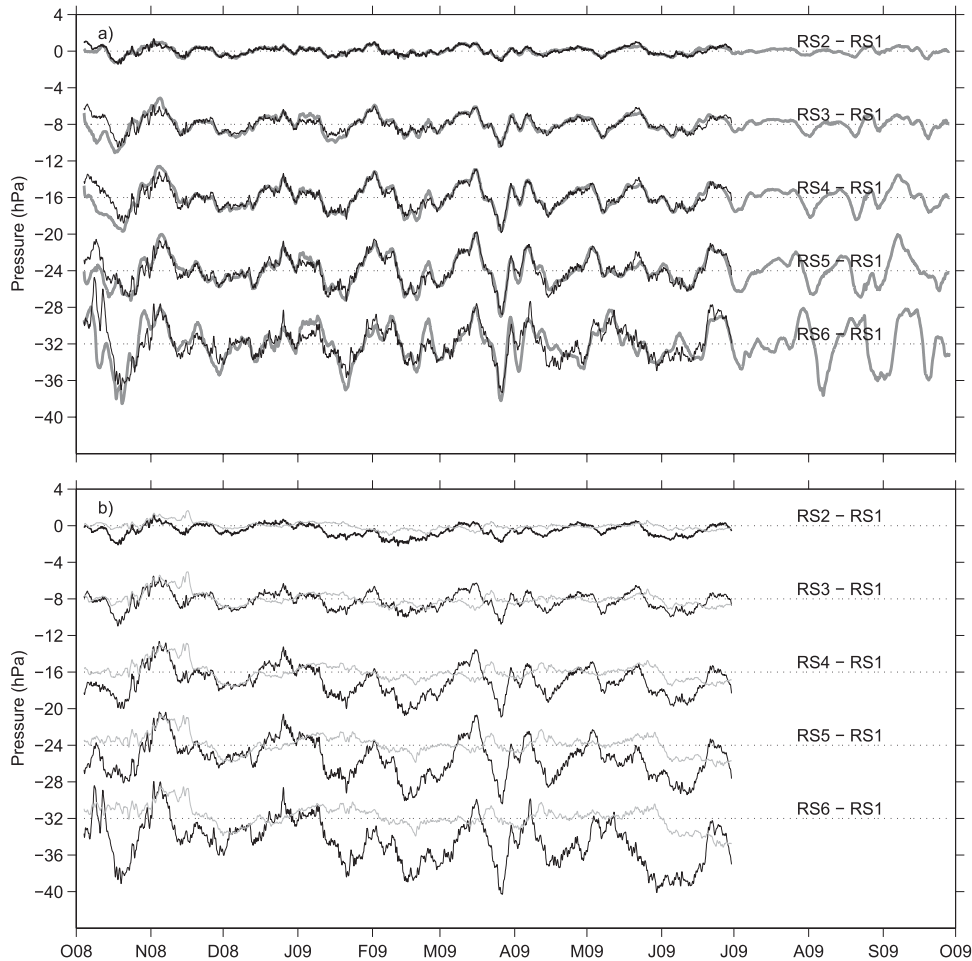


FIG. 10. (a) Pressure differences for RS2, RS3, RS4, RS5, and RS6 – RS1. All time series are bandpass filtered, passing periods of 1–50 days. Gray thick curves are from BPR data, and thin black curves are from method 1. Dotted lines show arbitrary offsets applied to the means. (b) The same pressure differences from method 1 but with a low-pass filter applied, passing all periods  $>1$  day. Black curves show the total pressure difference, and gray curves show the component due to density only.

We assume that the error in pressure from one measurement is a purely linear trend (here we choose RS1, though choosing RS2 instead produces very similar results). In Fig. 11 we show, for RS2, RS4, and RS5, the difference in pressure time series relative to RS1, after subtracting the dynamical signal as determined by the stepping method, but with no detrending applied to the BPR measurements. The fitted exponential-plus-linear trends clearly do a good job of explaining these instrumental errors, and there is rather little large-scale structure to the final residuals after subtracting these fitted trends, shown in the bottom panel. There remain hints of larger residuals in the first few weeks of the time series, and the exact time constants of the fitted exponentials do vary somewhat depending on which instrument is chosen to have a constant trend. We also

tried an iterative fitting method, in which an exponential-plus-linear trend was found for RS1 after fitting trends to the other time series, with this repeated starting with the new, detrended version of RS1 each time. This produced a very long time constant for RS1, effectively equivalent to fitting a quadratic trend, but it reduced the final residuals by only a very small amount.

The final residual variability noted on Fig. 11 is very similar to the values given in Table 3, despite including additional variability at periods longer than 50 days. There is certainly no structure in the final residuals in Fig. 11 of sufficient amplitude to justify the investigation of other forms of detrending function, though it is quite apparent that detrending is necessary, and that the functional form must involve monotonic curvature concentrated toward the start of the time

TABLE 3. Statistics of reconstruction by method 1 and method 2 for pairs of mooring from RS1 to the other moorings. Pairs for which data are complete with no known errors are marked in bold.

Pair	Method	Skill	Error (Pa)
<b>RS1,2</b>	1	0.84	16.68
	2	0.84	16.73
RS1,3	1	0.85	35.79
	2	0.85	35.27
<b>RS1,4</b>	1	0.92	36.77
	2	0.92	35.86
RS1,5	1	0.90	49.64
	2	0.90	49.90
RS1,6	1	0.69	100.24
	2	0.64	108.54

series, as provided for by the exponential-plus-linear form.

## 5. Summary and conclusions

For a boxlike ocean with vertical sidewalls, the application of thermal wind balance together with density measurements at the eastern and western boundaries of the ocean makes it possible to determine the geostrophic component of the MOC at a given latitude. In the real ocean, with sloping sidewalls, additional information is needed. Rather than follow the path of splitting the ocean into a boxlike interior region, for which thermal wind can be used and a separate slope region that must be measured separately, we demonstrate how the thermal wind concept can be extended to apply to integrals over more complex domains. This uses a generalization of hydrostatic balance for paths that are not vertical, given by (13), and shows how the geostrophic component of the MOC can be computed based on measurement of boundary values only. This requires, in addition to density measurements, measurements of the near-bottom current. Simple scale analysis shows that, for typical continental slope steepness, the accuracy required of current measurements (of order  $1 \text{ cm s}^{-1}$ ) is well within the capability of available instruments.

For the period October 2008 to September 2009, as part of the RAPID-WAVE experiment, we deployed instruments at six sites on the northwest Atlantic continental slope off Halifax, Nova Scotia, Canada, covering the depth range from approximately 1100 to 3900 m. With the data from these instruments, we were able to compute this generalization of the hydrostatic balance at the five steps between sites and to verify this computation with direct measurements of pressure differences. This comparison shows typical pressure mismatches

for a single 500–600 m step of 20–30 Pa, equivalent to 2–3 mm of water.

Although we find that density consistently plays a significant role in explaining the measured pressure differences, it is velocity that is responsible for most of the variability at the time scales accessible to study. This means that resolving the velocity structure over the continental slope is critical to success in monitoring zonally integrated transports. Density appears to play a relatively more important role at longer time scales, and it may well become the dominant signal for interannual variability. It is also worth noting that the relevant density signal, near the seafloor, shows quite different variability from that at the same depth but in open water above the deepest site RS6. Again, it remains to be seen whether this remains true at longer time scales, but it again emphasizes the importance of measuring right up to the boundary.

Unlike the direct pressure measurements, which suffer from significant long-term drifts, the indirect method using generalized hydrostatic balance is much more stable on long time scales. This makes it feasible to produce multiyear time series of the transport variability. The limiting factor for measurement accuracy appears to be the stability of salinity calibrations, which lead to density errors of about  $0.002 \text{ kg m}^{-3}$ , and hence pressure gradient errors of  $20 \text{ Pa km}^{-1}$ , an error that will be present in any measurement system that exploits thermal wind balance. Adding the effect of sampling and representation error, the stepping method leads to an accuracy equivalent to 0.82 Sv, for the zonally integrated flow between approximately 1100 and 3900 m, measured relative to 1100 m.

It is important to note that the measurements on the RS Line are not in themselves sufficient to calculate the complete overturning circulation at that latitude. What we have quantified in this paper are the zonally integrated transports and their errors, below and relative to 1100 m, on the assumption that changes in the bottom pressure gradient on the eastern boundary are negligible in that depth range. Any density changes and varying currents at the ocean floor on the deep eastern continental slope will also contribute to the zonally integrated meridional flow variability, as will any zonally integrated current at the chosen reference depth. A measurement of the full geostrophic overturning would require the method to be applied using data over the full depth range at both eastern and western boundaries.

With this paper, we introduce the RAPID-WAVE monitoring method and demonstrate that it works, and results in accuracy better than 1 Sv. Elsewhere (Elipot et al. 2013), we apply this method to demonstrate the

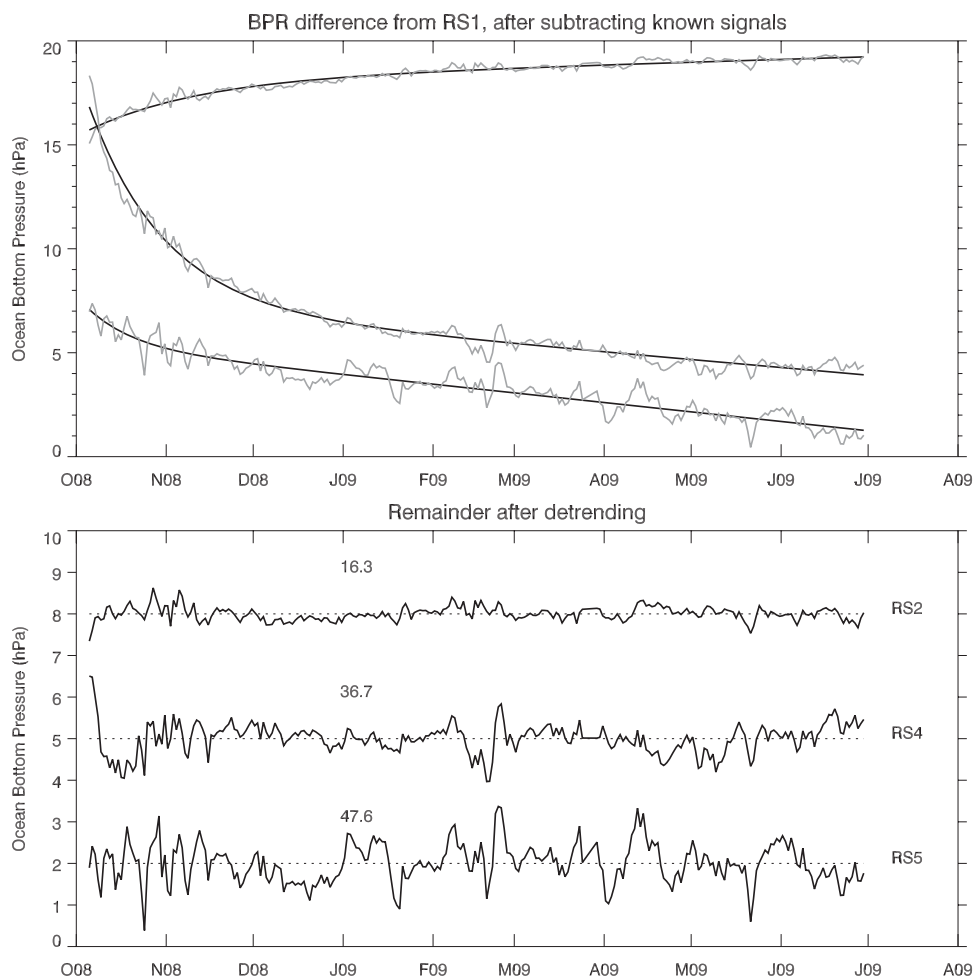


FIG. 11. Time series of pressure differences relative to RS1, as measured by BPRs at RS2, RS4, and RS5, following subtraction of the dynamical pressure signal reconstructed using the stepping method (method 1). (top) The complete time series with no detrending applied (gray) together with fitted exponential-plus-linear trends (black), with arbitrary vertical offsets (not shown). (bottom) Residuals after subtracting the fitted trends (arbitrary mean values shown as dotted lines). The numbers above each curve are standard deviations in pascals. All curves represent daily mean values, following the removal of tides.

degree to which coherent signals in the MOC can be seen across a range of latitudes. Future work will investigate the nature of that variability and its vertical structure in more detail.

*Acknowledgments.* This work was supported by the U.K. Natural Environment Research Council as part of the RAPID-WATCH project. Thanks to the technology groups at BIO and NOC for their development and/or preparation of the moorings and instruments used in the field program; to the scientific personnel, officers, and crew of the fall 2008 and 2009 CCGS *Hudson* expeditions for the successful execution of the program; and to Yuri Geshelin, Ed Horne, and Igor Yashayaev for their advice and assistance with the observations and/or data

processing. Conversations with Ric Williams were helpful in the development of this work.

## APPENDIX

### Extension of the Stepping Method for Complex Topography

Consider two measurements at  $y = 0$ ,  $x = x_1$  (in shallower water) and  $y = 0$ ,  $x = x_2$  (in deeper water). At these two points, we have measurements that tell us  $\nabla_h p_b$ , where  $\nabla_h$  is the horizontal gradient and  $p_b$  is the bottom pressure. The question is how best to use these values to calculate the pressure difference between the two points. Obviously, this involves some assumption

about the smoothness of the pressure gradient; otherwise (having no knowledge of the pressure gradient between the two measurement points), the interpolation would be impossible. Note that, throughout this appendix, we are assuming pressure values to be differences from a hydrostatically consistent reference profile, and similarly for density values wherever they are multiplied by  $g$  (the values are denoted  $p'$  and  $\rho'$  in the body of the paper), but we will drop the primes to avoid a clash of notation. In addition, throughout this appendix, the coordinate system is assumed to be rotated so that it is aligned with the particular pair of moorings considered, so that both lie on  $y = 0$ . We neglect the small effect of the changes in  $f$  that are implied by this when the pair of moorings is not at the same latitude.

If we have no other knowledge, then the simplest assumption is that the pressure gradient varies linearly in  $x$  and  $y$ , equivalent to assuming a quadratic variation of  $p_b$  in  $x$  and  $y$ :

$$p_b = ax + bx^2 + cxy + fy + gy^2, \quad (\text{A1})$$

which results in the components of the gradient

$$\frac{\partial p_b}{\partial x} = a + 2bx + cy, \quad \frac{\partial p_b}{\partial y} = cx + f + 2gy. \quad (\text{A2})$$

We can then calculate the pressure difference as

$$\delta p_b = p_{b2} - p_{b1} = \int_{x_1}^{x_2} \nabla p_b \cdot ds = \int_{x_1}^{x_2} \frac{\partial p_b}{\partial x} dx. \quad (\text{A3})$$

Performing the integral, this gives

$$\delta p_b = (x_2 - x_1)a + (x_2^2 - x_1^2)b = (x_2 - x_1)[a + b(x_2 + x_1)]. \quad (\text{A4})$$

Now, using an overline to represent the average of the two values at points  $x_1$  and  $x_2$ , application of (A2) at these two points (with  $y = 0$ ) allows us to write

$$\overline{\frac{\partial p_b}{\partial x}} = a + b(x_2 + x_1), \quad (\text{A5})$$

so that (A4) can be expressed as

$$\delta p_b = (x_2 - x_1) \overline{\frac{\partial p_b}{\partial x}}. \quad (\text{A6})$$

In other words, the assumption of quadratic variation in  $x$  and  $y$  leads to the intuitive result that the pressure difference is the difference in  $x$  multiplied by the average of the values of  $\partial p_b / \partial x$  measured at the two points.

This is the simplest form of the calculation, which should work in all cases as long as the spacing of the stations is small enough for the quadratic assumption to be valid.

For real station separations, it is possible for the topography between  $x_1$  and  $x_2$  to be quite complicated, such that it cannot be well approximated by a linear function. We expect that the flows are very strongly steered by topography, so complex topography would tend to lead to velocities that are not a linear function of  $x$  and  $y$ , thus reducing the accuracy of the interpolation. However, the strong topographic steering itself suggests a way of dealing with this.

Simple dynamical considerations (neglecting vertical velocity as a first approximation) lead to a flow that follows depth contours, and hence to a bottom pressure field that is purely a function of depth:  $p_b = p_b(H)$ . Within this approximation, the natural assumption of smoothness between the two measurement points, consistent with known pressure gradients at those two points, is that pressure should be a quadratic function of  $H$ :

$$p_b = a + bH + cH^2, \quad (\text{A7})$$

which leads to

$$\begin{aligned} \delta p_b &= b(H_2 - H_1) + c(H_2^2 - H_1^2) \\ &= (H_2 - H_1)[b + c(H_2 + H_1)]. \end{aligned} \quad (\text{A8})$$

Writing  $p'_b = dp_b/dH$ , we have  $p'_{b1} = b + 2cH_1$  and  $p'_{b2} = b + 2cH_2$ , so writing  $\overline{p'} = (p'_{b1} + p'_{b2})/2 = b + c(H_1 + H_2)$ , substitution into (A8) gives

$$\delta p_b = (H_2 - H_1) \overline{p'_b}. \quad (\text{A9})$$

In this case, instead of using the component of the pressure gradient that lies along the line between points 1 and 2, the interpolation is performed as a function of  $H$  and involves the component of pressure gradient that is perpendicular to the depth contours at each point.

For the case in which the depth is a linear function of  $x$  and  $y$  and  $p_b = p_b(H)$ , (A6) and (A9) are exactly equivalent. In that case,  $\partial H / \partial x$  and  $\partial H / \partial y$  are constants, so that  $(H_2 - H_1) = (\partial H / \partial x)(x_2 - x_1)$  and  $p'_b = (\partial p_b / \partial x) / (\partial H / \partial x)$ . In choosing between the different approaches, we are effectively making a choice between two approximations: is it better to assume that the points are so close together that the currents vary only linearly between them, or assume that the spatially coherent part of the flow is purely along depth contours? For a flow that is strongly steered by topography, we would expect the

second assumption to be better, although for closely spaced stations there should be very little difference.

To apply these approximations, we first have to relate the quantities in the formulas,  $\partial p_b/\partial x$  and  $p'_b$ , to the measured quantities, bottom density  $\rho$  and bottom velocity  $\mathbf{u}$ . Substituting geostrophic and hydrostatic balance into (A6), together with the matching assumption of constant slope, we obtain a formula for the pressure difference ignoring topographic steering, in terms of measured quantities:

$$\delta p = (x_2 - x_1)\overline{\rho f v} + (H_2 - H_1)\overline{\rho g}, \quad (\text{A10})$$

where the overline, as usual, represents the average of the values at stations 1 and 2.

For the case assuming dominance of topographic steering, using the generalized hydrostatic balance (13), we have

$$p' = \frac{\rho f u_L}{H_s} + g\rho, \quad (\text{A11})$$

where  $H_s$  is the (positive) gradient of  $H$  in the downslope direction and  $u_L$  is velocity along the slope with deep water to the right.

Now, substituting (A11) into (A9) gives a formula for the pressure difference with topographic steering, in terms of measured quantities:

$$\delta p = (H_2 - H_1) \left[ \overline{g\rho} + \left( \frac{\rho f u_L}{H_s} \right) \right]. \quad (\text{A12})$$

Finally, there is a possible way of combining the best qualities of the two methods, that is, using the knowledge that the primary pressure field is a function of depth but without throwing away the information about differences from that primary pressure field, which is available from the measurements in the form of the observed velocity perpendicular to depth contours. Whether this is an improvement over the assumption that  $p_b = p_b(H)$  depends on the extent to which violations of this assumption are geostrophic and coherent over the required length scales. If the flow perpendicular to the depth contours is not geostrophic or if it varies on very short length scales, then the ‘‘correction’’ suggested here will add noise to the estimate of pressure difference, rather than improving it.

Consider the situation shown in Fig. A1, in which the observations are at  $x_1$  and  $x_2$ , and the line  $\alpha\beta$  is the line of steepest descent between the depth contours on which the observations are made. In this situation, we could think of using  $p'_b$  to calculate the pressure difference between  $\alpha$  and  $\beta$  but using the velocity component

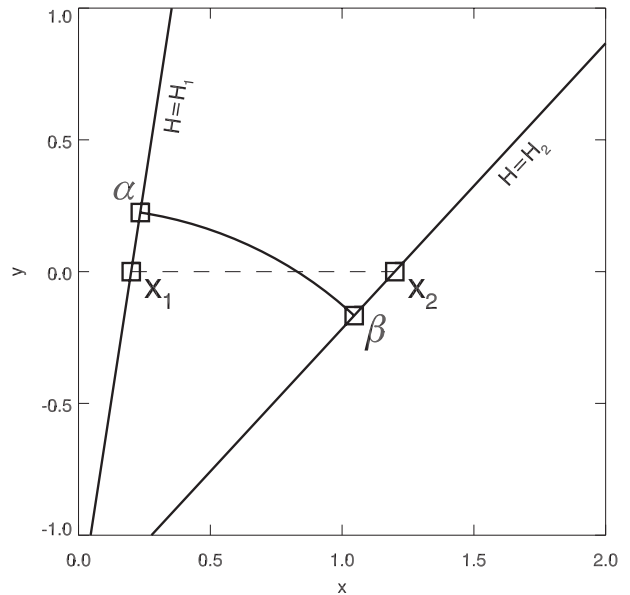


FIG. A1. Schematic of the geometry in a case with varying topographic gradient between the two observations.

normal to the depth contours to calculate the pressure differences between  $x_1$  and  $\alpha$  and between  $\beta$  and  $x_2$ .

Using geostrophy, the pressure difference between  $x_1$  and  $\alpha$  is

$$p_{b\alpha} - p_{b1} = -s_1(\rho f u_D)_1, \quad (\text{A13})$$

where  $u_D$  is the flow component perpendicular to the local depth contour (positive is toward deep water) and  $s_1$  is the distance along the depth contour from  $x_1$  to  $\alpha$  (the positive direction is with deep water to the right). Similarly, on the deeper contour,

$$p_{b2} - p_{b\beta} = -s_2(\rho f u_D)_2, \quad (\text{A14})$$

with  $s_2$  as the distance along the  $H_2$  depth contour from  $\beta$  to  $x_2$ .

Using the assumption that  $p_b$  is a smooth function of  $H$  along  $\alpha\beta$ , we can use (A12) to write

$$p_{b\beta} - p_{b\alpha} = (H_2 - H_1) \left[ \overline{g\rho} + \left( \frac{\rho f u_L}{H_s} \right) \right]. \quad (\text{A15})$$

Choosing  $s_1 = s_2 = S/2$ , the sum of (A13)–(A15) then leads to

$$\delta p_b = (H_2 - H_1) \left[ \overline{g\rho} + \left( \frac{\rho f u_L}{H_s} \right) \right] - S(\overline{\rho f u_D}), \quad (\text{A16})$$

where the final term involving  $S$  represents the correction that should improve on the assumption  $p = p(H)$ .

TABLE A1. Distance parameter  $S$  used for method 2e, as estimated from topography.

Pair	$S$ (m)
RS1,2	839
RS2,4	9498
RS2,3	6713
RS3,4	6973
RS4,5	4032
RS5,6	7404

In the case where  $H$  is a linear function of  $x$  and  $y$ , all  $H$  contours are parallel and are oriented at a constant angle  $\theta$ , say, to the positive  $x$  direction, and  $\alpha\beta$ , say, becomes a straight line of length  $D$ . Then we can write  $D = \delta x \sin\theta$  and  $S = \delta x \cos\theta$ , together with  $(H_2 - H_1)/H_s = D$ . Substituting these values then gives

$$\delta p_b = (H_2 - H_1)g\bar{\rho} + \delta x \sin\theta \overline{[\rho f u_L]} - \delta x \cos\theta \overline{[\rho f u_D]}. \quad (\text{A17})$$

Noting further that  $v = -u_D \cos\theta + u_L \sin\theta$  and that  $H_2 - H_1 = (\partial H/\partial x)\delta x$ , this becomes

$$\delta p_b = \delta x \left( \frac{\partial H}{g\bar{\rho}} \frac{\partial H}{\partial x} + \overline{\rho f v} \right), \quad (\text{A18})$$

which, for constant  $\partial H/\partial x$ , is precisely Eq. (A10), derived by assuming that the velocities are linear functions of  $x$  and  $y$ .

Thus, in (A16), we have an equation that both accounts for complex topography where it occurs (by using the assumption that pressure is approximately a quadratic function of depth) and reduces to the relation derived from the conventional assumption that velocities are linear functions of  $x$  and  $y$  in regions where  $H$  is a linear function of  $x$  and  $y$ .

In the paper, we refer to the simple method of (A10) as method 1, the method that assumes dominance of topographic steering given by (A12) as method 2, and the combined method of (A16) as method 2e. For method 2e we need an estimate of the along-slope offset  $S$ . This is chosen based on the offsets between lines of steepest descent illustrated in Fig. 6. For each instrument pair, there are two such offsets, one at the depth of each instrument. The average of the two is used to define  $S$ , except in the cases involving RS5, for which no estimate of downslope velocity is available. In the latter cases, we use asymmetrical calculations with  $s_1$  or  $s_2$  set to zero, as appropriate. An alternative of using the value of  $S$  that produces the best fit between pressure differences was also tried, but in no case did it give a significantly better result than that found by other methods. The derived distances  $S$  are listed in Table A1.

## REFERENCES

- Bingham, R. J., and C. W. Hughes, 2008: Determining North Atlantic meridional transport variability from pressure on the western boundary: A model investigation. *J. Geophys. Res.*, **113**, C09008, doi:10.1029/2007JC004679.
- Elipot, S., C. W. Hughes, S. C. Olhede, and J. M. Toole, 2013: Coherence of western boundary pressure at the RAPID WAVE array: Boundary wave adjustments or deep western boundary current advection? *J. Phys. Oceanogr.*, in press.
- Hughes, C. W., and B. A. de Cuevas, 2001: Why western boundary currents in realistic oceans are inviscid: A link between form stress and bottom pressure torques. *J. Phys. Oceanogr.*, **31**, 2871–2885.
- Johns, W. E., L. M. Beal, M. O. Baringer, J. R. Molina, S. A. Cunningham, T. Kanzow, and D. Rayner, 2008: Variability of shallow and deep western boundary currents off the Bahamas during 2004–05: Results from the 26°N RAPID–MOC array. *J. Phys. Oceanogr.*, **38**, 605–623.
- Kanzow, T., U. Send, W. Zenk, A. D. Chave, and M. Rhein, 2006: Monitoring the integrated deep meridional flow in the tropical North Atlantic: Long-term performance of a geostrophic array. *Deep-Sea Res. I*, **53**, 528–546.
- , H. L. Johnson, D. P. Marshall, S. A. Cunningham, J. J.-M. Hirschi, A. Mujahid, H. L. Bryden, and W. E. Johns, 2009: Basinwide integrated volume transports in an eddy-filled ocean. *J. Phys. Oceanogr.*, **39**, 3091–3110.
- Loder, J. W., C. G. Hannah, B. D. Petrie, and E. A. Gonzalez, 2003: Hydrographic and transport variability on the Halifax section. *J. Geophys. Res.*, **108**, 8003, doi:10.1029/2001JC001267.
- Lozovatsky, I. D., and S. M. Shapovalov, 2012: Thickness of the mixed bottom layer in the northern Atlantic. *Oceanology*, **52**, 447–452, doi:10.1134/S0001437012010134.
- Marsh, R., B. A. de Cuevas, A. C. Coward, J. Jacquin, J. J.-M. Hirschi, Y. Aksenov, A. J. G. Nurser, and S. A. Josey, 2009: Recent changes in the North Atlantic circulation simulated with eddy-permitting and eddy-resolving ocean models. *Ocean Modell.*, **28**, 226–239, doi:10.1016/j.ocemod.2009.02.007.
- Rayner, D., and Coauthors, 2011: Monitoring the Atlantic meridional overturning circulation. *Deep-Sea Res. II*, **58**, 1744–1753, doi:10.1016/j.dsr2.2010.10.056.
- Schott, F. A., J. Fischer, M. Dengler, and R. Zantopp, 2006: Variability of the deep western boundary current east of the Grand Banks. *Geophys. Res. Lett.*, **33**, L21S07, doi:10.1029/2006GL026563.
- Send, U., M. Lankhorst, and T. Kanzow, 2011: Observation of decadal change in the Atlantic meridional overturning circulation using 10 years of continuous transport data. *Geophys. Res. Lett.*, **38**, L24606, doi:10.1029/2011GL049801.
- Smith, W. H. F., and D. T. Sandwell, 1997: Global sea floor topography from satellite altimetry and ship depth soundings. *Science*, **227**, 1956–1962.
- Toole, J. M., R. G. Curry, T. M. Joyce, M. McCartney, and B. Penamolino, 2011: Transport of the North Atlantic deep western boundary current about 39°N, 70°W: 2004–2008. *Deep-Sea Res. II*, **58**, 1768–1780, doi:10.1016/j.dsr2.2010.10.058.
- Watts, D. R., and H. Kontoyiannis, 1990: Deep-ocean bottom pressure measurement: Drift removal and performance. *J. Atmos. Oceanic Technol.*, **7**, 296–306.
- Wunsch, C., 2008: Mass and volume transport variability in an eddy-filled ocean. *Nat. Geosci.*, **1**, 165–168, doi:10.1038/ngeo126.